Results

3.1 Sample Preparation

Because of the slightly different setups used during synchrotron and UHV studies, two different methods of sample preparation were applied.

3.1.1 CLEANING

SYNCHROTRON PROCEDURES — The electrodes (polycrystalline gold foil, thickness 0.1 mm, purity 99.99%) were treated with 65 % nitric acid and afterwards with a 1:1 mixture of 25 % ammonia and 30 % hydrogen peroxide. The cleaning procedure was finished with careful rinsing of the sample with triply distilled water. All glass parts used at the synchrotron were cleaned in hot 65 % nitric acid for 24 hours and were afterwards carefully rinsed with triply distilled water to remove all organic and ionic residuals. The electrolyte was prepared from 70 % ultrapure perchloric acid (Merck) and triply distilled water. After mounting the sample, the whole system was kept under Helium (purity: 4.6) as inert gas atmosphere. Helium is applied because of its low absorption in the X-ray regime. It is therefore better suited than e.g. nitrogen or argon. Furthermore, in total electron yield measurements, Helium enhances the ion yield *via* secondary processes. The sample current is enhanced and the S/N ratio improves.

UHV PROCEDURES — The electrode was exposed to sputter-heat cycles to remove surface contaminants. A typical cycle consisted of heating the sample to 800 K for 10 minutes during Ar sputtering (p_{Ar} = 5*10^{-4} mbar, E = 500 eV) and then sputtering another 20 minutes at room temperature. The cleaning methods described in [20, 50] are more gentle as these studies deal with single crystal surfaces which can be damaged using the cleaning procedures described here. Damage to the sample by exposing it to the Ar beam at high temperatures is unlikely here, as a polycrystalline gold foil has been used which is not sensitive to this kind of damage. The samples were

afterwards characterised *via* XPS to be sure no carbon or oxygen resided on the surface. Special care was taken to ensure the absence of calcium from the surface. Canning *et al.* [10] discusses the change in the adsorption behaviour of oxygen on gold by calcium impurities. Such impurities have never been observed in this study which might be due to the fact that extremely thin gold foils and not single crystals were used. Even tempering the sample at 700 K in oxygen atmosphere yielded no detectable amounts of Ca in XPS experiments. The clean electrode was transferred to the electrochemical cell, which was constantly purged with nitrogen (purity: 5.0). The electrochemical cell was cleaned exactly as described for the synchrotron cell.

3.1.2 PREPARATION OF THE AU/O PHASES

BY SPUTTERING WITH OXYGEN PLASMAS —   A Penning type sputter gun (Leybold) was used for generating a plasma discharge. The dependence of the discharge current on the different sputtering parameters were investigated. Fig. 3.1 shows a typical current response to a 60 s plasma discharge applying 250 V acceleration voltage. Throughout the experiments it has been found that the sample current depended strongly on the partial pressure of O_2. The acceleration voltage influenced the sample current only weakly. The O_2 plasma discharge ignited at an oxygen partial pressure of $8 \cdot 10^{-3}$ mbar. Below this value, the maximum achievable sample current was about 6 μA rising to approximately 60 μA at the value mentioned.

BY ELECTROCHEMICAL OXIDATION —   All electrochemical experiments at the UHV chamber have been carried out using the electrochemical cell shown in fig. 2.15. Electrochemical oxidation during synchrotron work has been done in a typical three electrode cell as described in the literature [23–25]. The potentiostat/galvanostat used was an AMEL model 2051. This instrument is capable of maintaining voltages up to ± 10 V or currents up to $\pm$ 1 A during the experiments. In this thesis, galvanostatically and potentiostatically prepared O/Au phases have been characterised. In figs. 3.2 (a) and (b) typical current/time and potential/time responses are shown for an oxidation in the potentiostatic and the galvanostatic case. It should be mentioned that the current response to a given potential step changes drastically when increasing the potential above a certain threshold value. If U_{ox} is chosen to be smaller than 1.6 V, the current rises to a peak value and then rapidly drops while above 1.6 V, the current stays nearly constant all the

Figure 3.1: Typical sample current during a plasma discharge oxidation:
The discharge current inhomogeneities are due to pressure changes in the preparation chamber. A given pressure value is not stable after discharge ignition - it rises a few percent. Therefore, one has to regulate the pressure constantly which gives rise to the pressure changes.
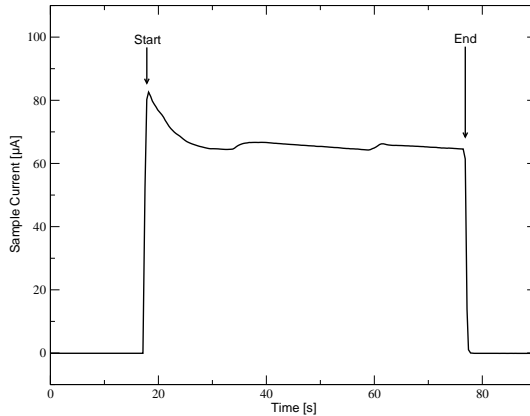

time. This behaviour is in good agreement with the literature where different oxidation stages are proposed while increasing the oxidation potential. At low potentials, OH adsorption and monolayer oxidation take place. These processes passivate the surface, i.e. the current has to drop if a certain surface concentration of OH or O is achieved and no more adsorption can take place (monolayer population). If one further increases the oxidation potential, gold oxidation as well as gold dissolution occurs. As a result, the formed passivation layers are constantly broken up giving the oxygen access to bulk gold atoms ("blister" mechanism of the oxidation process). To evaluate the portion of charge which is responsible for the oxidation process, redox cycles have been done where the ratio between Q_{ox} and Q_{red} is plotted against the charge flown through the system. This graph is shown in fig. 3.3. From this graph it can be seen that except for low amounts of charge passing through the system (i.e. monolayer oxidation or OH adsorption) only about one percent of the total charge is used for oxidising the gold surface. Therefore, it can be estimated that the surface is constantly roughened during oxidations where large amounts of charge pass through the sample because of the high contribution of Au dissolution to the total process. In fig. 3.4 some

Figure 3.2: Examples for the galvanostatic and potentiostatic oxidation processes.
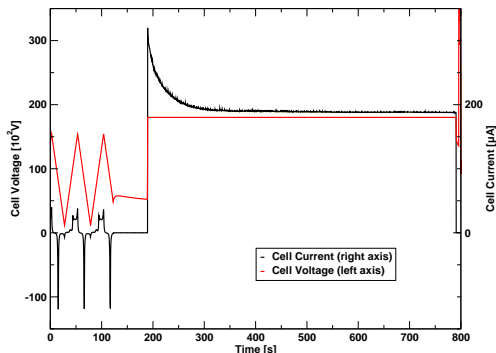

(a) An example for potentiostatic oxidation. In the left part, the current/time and potential/time course for some cyclic voltammograms is visible. These are always included to check the surface state immediately before oxidation. At t=120 s, the potentiostat is switched off (current falls to 0), the parameters for the oxidation are adjusted (here: U_{ox}=+1.8V) and at t=200s, the potentiostat is switched on. See text for further discussion of the current/time evolution.
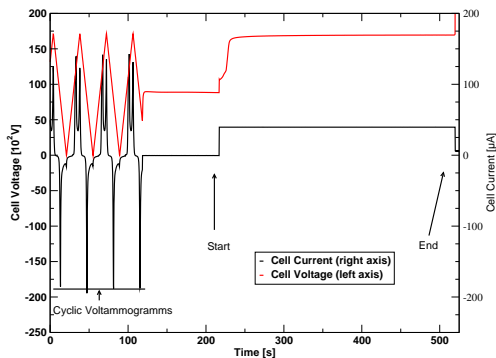
(b) An example for galvanostatic oxidation. See the discussion of the left figure for further details. The only difference is the working mode of the potentiostat.

Figure 3.3: Ratio between Q_{ox} and Q_{red} related to the oxidation charge. The figure shows a nearly constant value (about 1%) above 25 C of flown charge. In the region below this value, higher values can be observed. All values here are taken in potentiostatic experiments.
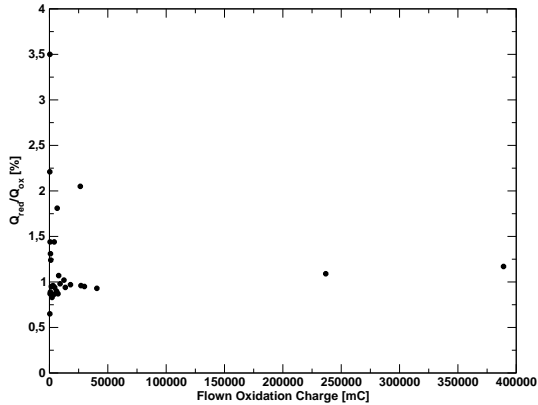
selected reduction peaks used for this evaluation are shown. To evaluate

Figure 3.4: Evolution of reduction peaks on a polycrystalline gold surface as a function of oxidation potential. As can be seen, the minima shift to lower potentials with increasing potential. The inlay shows the low potential region in more detail.
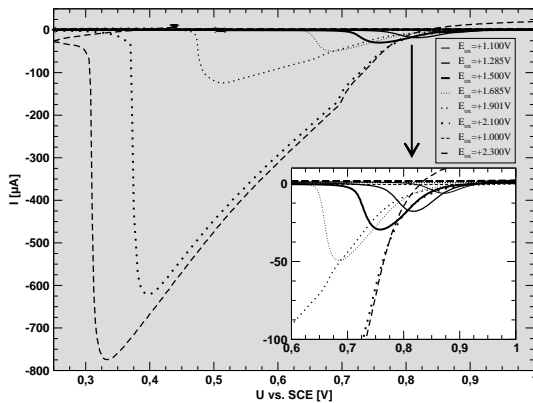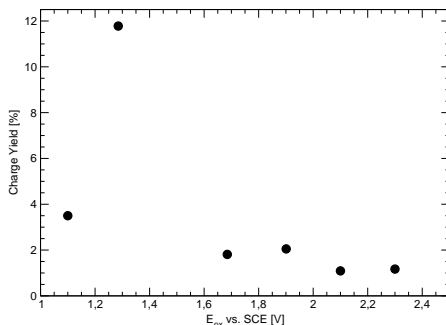
Figure 3.5: Integral of the reduction peak as a function of the oxidation potential U_{ox}. The passing through a maximum is obvious and has been verified in control experiments.


the influence of the oxidation potential on the total charge yield of the oxidation process, additional potentiostatic experiments have been carried out. The sample was oxidised for 300 s at a given potential and the reduction signal was integrated. From this experiment one can deduce that the charge yield passes through a maximum value which lies at +1.3 V vs. SCE. This can be understood when recapitulating the electrode processes which are responsible for the current flow. At potentials below 1.3 V, only passivation (i.e. monolayer oxidation) of the surface takes place. Above 1.6 V, oxygen evolution and gold dissolution are more and more favoured, the oxidation becomes a side effect. It is therefore not surprising that fig. 3.5 shows a maximum value at +1.3 V. The maximum value in this graph represents the point where bulk oxidation is already possible (and not only monolayers of Au_2O_3 are formed) but where gold dissolution and oxygen evolution are still disfavoured.

Fig. 3.6 shows the relation between oxidation charge and oxide thickness measured in the potential range where the oxidation current stays constant over the oxidation time. For all potentials measured, a linear relation between oxidation and reduction charges can be observed, which is in line with the literature. From the reduction charge, the number of Au particles reduced in the procedure (i.e. the number of Au^{3+} ions formed during oxi-

dation) can be measured. A growth constant k=1.2·10^{-2} [Particles·scm/mC] can be obtained *via* linear regression of the data in the upper right graph. This value will be confirmed *via* EXAFS measurements in the following chapters.

Figure 3.6: Relation between oxidation charge and number of reduced Au ions. In the potential range investigated here, a linear relationship can be established. It should be noted that the potential range chosen is above the previously mentioned critical potential above which the oxidation current stays constant during the experiment.
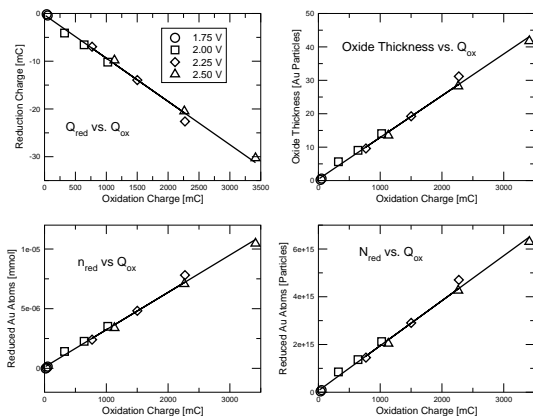

3.2 XAS Experiments

3.2.1 DETERMINATION OF S_0^2 FOR CRYSTALLINE AND AMORPHOUS GOLD OXIDES

The overall amplitude reduction factor is usually included as a parameter in the EXAFS fitting procedure. If one fits coordination numbers and S_0^2 in the same fit, both parameters show a high correlation. This is due to the fact that FEFFIT includes both parameters as a simple product function. Therefore it is worthwhile determining one of the two parameters in advance. S_0^2 can be evaluated according to a method proposed by Ravel [63]. Ravel's method works in any case where the first shell contributions in the Fourier transform can be well separated from the other shells. In this case, one carries out

Figure 3.7: Determination of S_0^2 for different samples:
The plot of σ^2 vs. S_0^2 yields three straight lines which intersect in a triangular
pattern. The midpoint of these triangles is taken to be S_0^2. The upper curve
shows the determination of S_0^2 for Au metal, the lower curve for electrochem-
ically prepared Au_2O_3. Crystalline Au_2O_3 shows the same behaviour as the
metal.
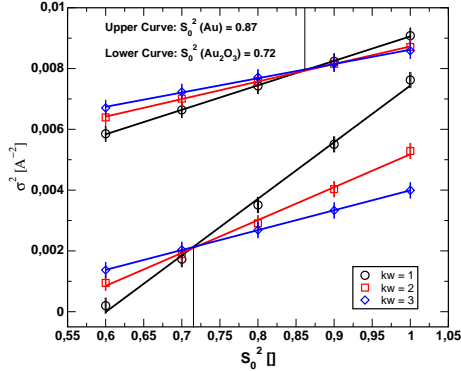
different fits of the first shell parameters (i.e. E_0, σ^2, N, ΔR) for fixed values
of S_0^2. This procedure is repeated for a k-weighting of one, two and three.
Plotting the fitted values of σ^2 vs. the fixed S_0^2 yield three straight lines with
different slopes which should ideally intersect in one point which represents
the S_0^2 parameter that best fits the system. If the lines do not intersect in a
point but in a triangular pattern, the midpoint of this triangle can be taken
to be S_0^2. Using this method has the advantage that one does not need to
include S_0^2 as a parameter in further fitting routines. This gives better fitting
results in cases, where one needs to fit coordination numbers. This method
has been applied to electrochemically grown and hydrothermally prepared
Au_2O_3 and is shown in fig. 3.7. As can be seen, the crystalline material
shows a significantly higher S_0^2 value. This generally suggests a larger de-
gree of order in the sample as S_0^2 accounts for amplitude reduction due to
sample inhomogeneities and non-Gaussian disorder. S_0^2 values of crystalline
materials usually lie between 0.8 and 0.95. The deviation from this range for
the electrochemically prepared material can be attributed to a much higher
disorder here than in commonly investigated samples like metals or single
crystals. The S_0^2 values are well in line with the other fitting parameters.

### 3.2.2 EXPERIMENTS WITH CRYSTALLINE Au_2O_3 - A REFERENCE COMPOUND

Samples containing crystalline Au_2O_3 were prepared by hydrothermal synthesis as described previously [2, 35]. Briefly, a pressure of 3000 bar and a temperature of 600 K was applied to a 1M solution of $HAuCl_4$ for 6 weeks using an autoclave. This treatment resulted in a mixture of crystalline Au_2O_3 and metallic Au. An XRD-analysis (Stoe powder diffractometer, Bragg-Brentano geometry) of the sample indicated that it contained approximately 80 mol% Au_2O_3 (fig. 3.8(a)) and 20 mol% Au. A linewidth analysis of the pattern using the Scherrer formula indicated crystallite sizes of approximately 20 nm. No indications for preferred orientation or texturisation of the crystallites were detectable.

For the Au L_3-edge EXAFS measurements, the sample was diluted in boron nitride. Measurements were taken in transmission mode (setup shown in fig. 2.11), adjusting the thickness of the BN mixture so that an edge step of 1.2 resulted. Because XRD indicated that 20 atom% of all Au in the sample was present as metallic Au, this contribution to the EXAFS spectrum needed to be eliminated by subtraction of a standard Au metal spectrum. To this end, the L3-edge spectrum of a 5 μm thick gold foil was measured under the same conditions as the Au_2O_3 sample.

Throughout the XAS measurements, the double-crystal Si(311) monochromator was kept detuned at 60% of maximum reflectivity to suppress harmonics in the X-ray beam. Ion chambers were used to determine the intensity of the incoming and the transmitted beam, with pure nitrogen in the ion chamber for the incoming and pure argon in the ion chamber for the transmitted beam. During measurements, the synchrotron storage ring DORIS operated in multi-bunch mode, with ring currents between 80 mA and 100 mA. Data acquisition times for one spectrum were about half an hour.

Data analysis was performed using the full multiple scattering code FEFF8 to calculate backscattering matrices [1]. The AUTOBK code [55] was used to subtract the atomic background functions from the raw absorption spectra and to calculate the EXAFS by normalisation to the absorption edge step height. FEFFIT [54] was used to fit scattering contributions.

Figure 3.8: Pre characterisation of the crystalline gold oxide sample.
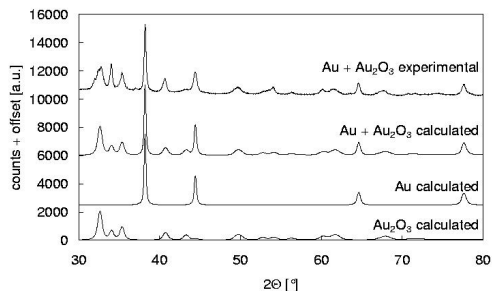
(a) XRD analysis of the sample containing 80% Au_2O_3 and 20% Au. The upper pattern is the experimental pattern obtained for the sample used for the EXAFS analysis. The pattern below this is the one calculated with the PowderCell code. It is a linear combination of the two reference patterns (Au and Au_2O_3) which are shown at the bottom of the figure.
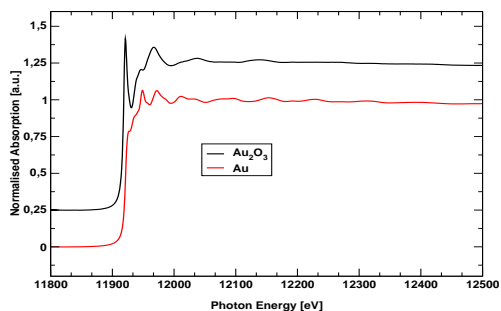
(b) Raw Au L_3-edge X-ray absorption spectrum of Au and Au_2O_3. The differences in the XANES region which are mainly due to the difference in the electronic structure of the materials are clearly visible. The whiteline in the Au_2O_3 spectrum comes from 6s $\longrightarrow$ 5d transitions.

3.2.3 EXAFS ANALYSIS OF CRYSTALLINE Au_2O_3

Raw Au L_3-spectra of the Au_2O_3 sample and the Au foil are given in fig. 3.8(b). To identify the contribution of Au metal to the EXAFS of the Au_2O_3 sample, a single scattering analysis of the EXAFS spectrum, including only the paths for single scattering from the nearest neighbours of Au in the oxide (4 O atoms at 2.00 Å) and in the metal (twelve Au atoms at 2.92 Å) has been carried out. This simple procedure is appropriate because the scattering contributions from the nearest neighbours in both structures are well separated from those of all other scattering paths, as is easily seen by examining the Fourier transformed EXAFS spectra of Au metal and the Au_2O_3 sample (fig. 3.10). The single scattering analysis was thus carried out by fitting to Fourier-filtered EXAFS spectra obtained by applying a Fourier window with Hanning boundaries centred at 1 Å and 3 Å respectively. The results are given in table 3.1. The fraction of Au_2O_3 contributions in the sample was

Table 3.1: Phase composition analysis using EXAFS.

Statistical Parameter	Value		Parameter	Physical Interpretation	Value	Error
Independent Points	15		ΔE_{Au}	Fermi energy shift in Au-reference	-4.99	4.88
Number of Variables	7		ΔE_O	Fermi energy shift in O-reference	16.67	1.26
Degrees of Freedom	8		σ^2_{Au}	Debye Waller Factor (Au-Atoms)	0.006	0.001
R-factor of Fit	0.021		σ^2_O	Debye Waller Factor (O-Atoms)	0.003	0.0005
χ^2	294		ΔR_{Au}	deviation from ideal position (Au)	-0.02	0.005
reduced χ^2	36.21		ΔR_O	deviation from ideal position (O)	0.040	0.003
k Interval	[3:18]		P_{ox}	oxide contribution to EXAFS	0.84	0.04
R Interval	[1:3]					

(b) Variables used in the fit.

(a) Statistical Parameters.

found to be 84±4 % which is in good agreement with the result of the XRD analysis. The agreement between the phase analyses obtained with a long-range (XRD) and a short-range (EXAFS) probe indicates that XRD-invisible (ämorphous") components in the sample were at most a few atom%. The influence of highly disordered sample contributions without long-range order, or of small Au and/or Au_2O_3 crystallites with diameters below a few nm can thus be assumed as negligible within the sensitivity level of EXAFS (a few %). The absorption spectrum of Au_2O_3 was subsequently obtained

by taking the edge-step normalised absorption spectra of the Au_2O_3 sample and of the Au foil reference, scaling the latter by the weighting factor obtained from the phase analysis (16%), and subtracting it from the spectrum of the Au_2O_3 sample. In fig. 3.9, the resulting Au_2O_3 near-edge spectrum (re-normalised to the edge-step height) and its EXAFS are compared to the respective parent spectra. The results of a full multiple scattering (FMS) ana-

Figure 3.9: Phase analysis of Au_2O_3: The difference in the XANES and EXAFS Region of raw and processed data are shown. In particular, the EXAFS shows significant changes after processing the data in the manner described.
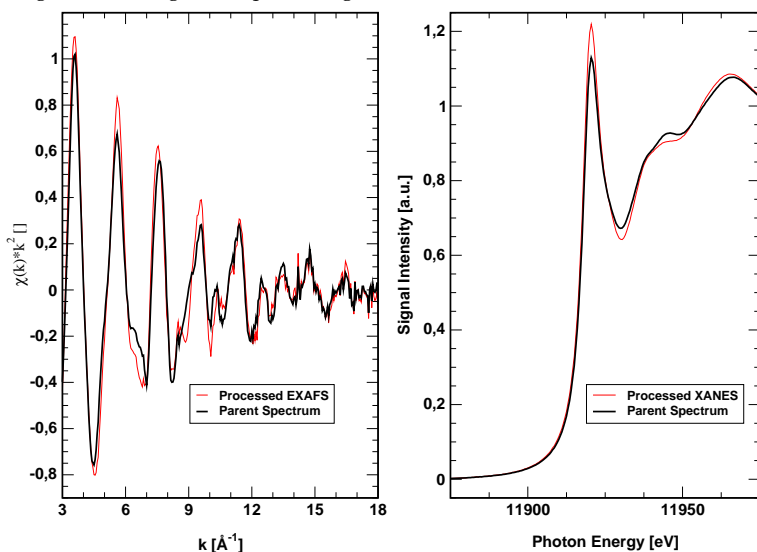

lysis of the Au_2O_3 EXAFS are shown in fig. 3.10(a) and tables 3.2(a) and (b). A drawing of the unit cell of Au_2O_3 indicating the atoms included in the fit to the experimental data is given in figure 3.10(b). The FMS calculation of the Au EXAFS was performed using the crystallographic structure reported in references [35, 37]. All scattering paths up to 4 Å length were taken into account. Table 3.3 summarises the properties of all scattering paths contributing to the EXAFS with an intensity of at least 3% of the most intense scattering path, which derives from backscattering at the most tightly bound, nearest oxygen atom (distance: 1.93 Å). The results of the calculation pre-

Figure 3.10: Results of the EXAFS analysis of Au_2O_3.
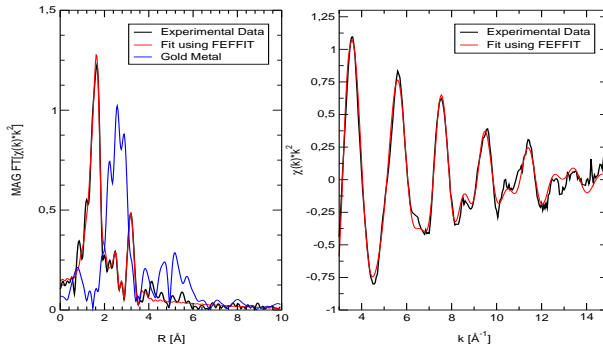
(a) EXAFS Fit:

The fit performed with the FEFFIT algorithm shows good agreement between experimental data and theory. The left figure shows the Fourier transformed EXAFS functions of gold oxide (experiment and theory) and gold metal for comparison. The separation of the first shell contributions between gold and gold oxide is clearly visible, making a determination of S_0^2 according to Ravel possible.
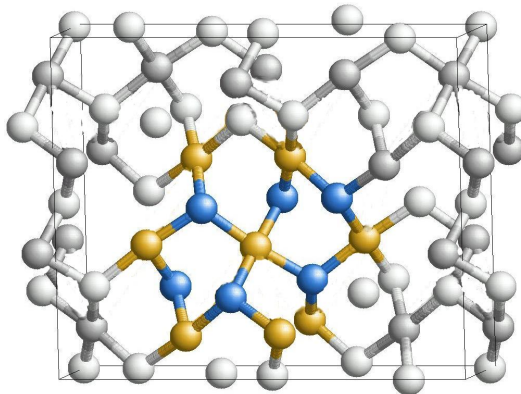
(b) Corresponding Structural Model:

The yellow atoms correspond to gold, the blue ones to oxygen atoms. Dark shaded atoms reflect gold atoms in the unitcell which are not covered by the EXAFS analysis. The same is true for the light shaded balls and oxygen.

Table 3.2: Results of the full EXAFS analysis of Au_2O_3.

Statistical Parameter	Value	General Parameters					
		S_0^2	0.83			E_0	16.08
Independent Points	39.500						
Number of Variables	23						
Degrees of Freedom	16.5		Path Parameters				
R-factor of Fit	0.022						
χ^2	1104.60	Atoms	Type	R_{nom}	ΔR	σ^2	N
reduced χ^2	27.96		single or multiple scattering	ideal distance from absorber	distance deviation	Debye Waller Factor	Degeneracy
k Interval	[3:18]						
R Interval	[1:5]						
		Au,O	SS	1.929	0.075	0.004	4
(a) Statistical Parameters.		Au,O	SS	2.814	0.031	0.005	1
		Au,O	SS	2.904	0.031	0.005	1
		Au,Au	SS	3.033	0.005	0.006	1
		Au,O	SS	3.049	0.073	0.003	1
		Au,Au	SS	3.337	0.020	0.006	2
		Au,Au	SS	3.351	0.050	0.007	2
		Au,Au	SS	3.459	0.026	0.007	2
		Au,O	MS	4.001	-0.006	0.002	2

(b) Variables used in the fit.

dict that only one multiple scattering path contributes to the EXAFS with an intensity of significantly more than 10% of the strongest scattering path: it is a triangular scattering path involving the nearest oxygen atom and the less tightly bound oxygen atom closest to it. All other multiple scattering paths, including the ping-pong"double scattering path to the nearest neighbour (path 25) have much lower relative intensities, which never exceed approximately 12%. In contrast, no single scattering path with a length below 3.85 Å has an amplitude of less than approximately 30%. The theoretical analysis of electron backscattering in Au_2O_3 thus predicts that a fitting analysis of the experimental EXAFS including only single-scattering paths (and possibly the mentioned most intense multiple scattering path) should be successful. To check this prediction the fitting analysis of the experimental spectrum was performed using the calculated scattering matrices. The results are given in table 3.2(b). In agreement with the prediction of the theoretical analysis good agreement between calculation and experiment upon inclusion of all single scattering paths with lengths below 3.85 Å was found. The overall amplitude factor S_0^2 has been kept fixed to the value determined earlier.

Table 3.3: Theoretical fitting standards obtained with the FEFF8 code (Parameters: EDGE=L3, S02=1.0, EXAFS, RPATH=8.85):
The values show a good correlation between theoretically calculated path intensity and the importance of a path in the fit. Note that all single scattering paths up to 3.8 Å were included in this fit. The EXAFS function is clearly dominated by these single scattering contributions.

Path Nr.	Degeneracy	R_{eff}	Calc. Intensity	Included in fit	Contributing Atoms	Type of Path
0001	1	1.929	100.00	yes	Au O Au	single
0002	1	2.012	90.93	yes	Au O Au	single
0003	1	2.042	87.92	yes	Au O Au	single
0004	1	2.071	85.08	yes	Au O Au	single
0005	1	2.814	39.50	yes	Au O Au	single
0006	1	2.904	36.29	yes	Au O Au	single
0007	1	3.033	38.72	yes	Au Au Au	single
0008	1	3.049	31.72	yes	Au O Au	single
0009	1	3.193	27.86	no	Au O Au	single
0010	2	3.337	64.14	yes	Au Au Au	single
0011	2	3.351	63.55	yes	Au Au Au	single
0012	2	3.352	11.44	no	Au O O Au	multiple
0013	2	3.355	12.09	no	Au O O Au	multiple
0014	2	3.446	3.79	no	Au Au O Au	multiple
0015	2	3.459	59.40	yes	Au Au Au	single
0016	2	3.481	10.34	no	Au O O Au	multiple
0017	2	3.559	10.22	no	Au O O Au	multiple
0018	2	3.703	4.27	no	Au Au O Au	multiple
0019	2	3.703	4.36	no	Au Au O Au	multiple
0020	2	3.710	3.81	no	Au Au O Au	multiple
0021	2	3.710	3.95	no	Au Au O Au	multiple
0022	2	3.787	4.41	no	Au Au O Au	multiple
0023	2	3.787	4.50	no	Au Au O Au	multiple
0024	2	3.838	46.88	no	Au Au Au	single
0025	1	3.858	8.12	no	Au O Au O Au	multiple
0026	1	3.892	15.50	no	Au O Au	single
0027	1	3.894	15.47	no	Au O Au	single
0028	1	3.911	15.27	no	Au O Au	single
0029	1	3.973	14.54	no	Au O Au	single
0030	2	3.997	21.15	no	Au O O Au	multiple
0031	2	4.001	50.34	yes	Au O Au O Au	multiple
0032	1	4.025	6.69	no	Au O Au O Au	multiple
0033	2	4.053	20.18	no	Au O O Au	multiple
0034	2	4.055	48.27	no	Au O Au O Au	multiple
0037	1	4.084	6.25	no	Au O Au O Au	multiple
0043	1	4.143	5.85	no	Au O Au O Au	multiple
0044	1	4.248	11.76	no	Au O Au	single
0045	2	4.304	4.27	no	Au O O Au	multiple
0046	2	4.312	35.10	no	Au Au Au	single
0047	1	4.331	11.06	no	Au O Au	single
0048	2	4.397	33.38	no	Au Au Au	single
0049	2	4.407	3.44	no	Au O O Au	multiple
0050	2	4.421	2.71	no	Au O O Au	multiple

Adding the most intense multiple-scattering path in the fitting procedure improved agreement between calculated and experimental data somewhat, but all other scattering paths turned out to be insignificant. The values obtained for the Debye-Waller factors (σ^2) are within reasonable limits. In line with the good crystallinity of the sample, as indicated by the XRD diagram, use of the cumulant expansion for the contributions of disorder did not improve the fit quality significantly. Another indication for an insignificant disorder level is the value of 0.82 for the overall amplitude factor S_0^2, which is, within error limits, comparable to values obtained for other crystalline systems. A list of all scattering paths calculated by FEFF is given in tab. 3.3. The unusually strong dominance of single-scattering contributions to the EXAFS reflects the fact that the relatively open and complicated network structure of Au_2O_3 is characterised by a low local symmetry around the Au absorbers (the unit cell has dimensions of 50 x 40 x 30 nm). As a result, there are no multiple scattering paths with high degeneracy levels as, e.g., in cubic oxides with the NaCl structure. For a comparison, in fig. 3.11 fits of crystalline Au_2O_3 are shown with and without including single scattering paths. The upper graphs (single scattering) show a good agreement between experiment and theory in the range from 1 to 2.8 Å. The only difference between the two fits is that the peak at 3.2 Å in the Fourier transformed spectra is better fitted when using multiple scattering paths.

3.2.4   EXAFS ANALYSIS OF ELECTROCHEMICALLY GROWN Au_2O_3

Having discussed the properties of crystalline Au_2O_3 we now turn to the analogous electrochemical compound. Comparing the Fourier transformed EXAFS of the grown oxide films with hydrothermally prepared gold(III) oxide the high disorder in the electrochemically grown oxide becomes apparent. While the hydrothermally grown oxide shows strong contributions at high r-values, the spectrum of electrochemically grown oxide only shows a broad peak which can be attributed mainly to the first oxygen scatterers. The analysis parameters of this fit are shown in tables 3.4 (a) and (b), figure 3.12(a) shows the experimental and simulated data in k, r and back-transformed k space. The structural unit elucidated is shown in fig. 3.12(b). As one can see, the EXAFS signal is dominated by the contributions of the first four oxygen atoms, which are arranged in a distorted square planar geometry around the gold absorber. Additionally, a second gold and a second oxygen absorber can be detected as 2nd and 3rd shell, respectively. As the

Figure 3.11: Comparison between single- and multiple scattering fits for Au_2O_3. The fit shows a good agreement between theory and experiment in the whole fitting range (k-Interval: [3:18] Å^{-1}, r-Interval: [1:5] Å).
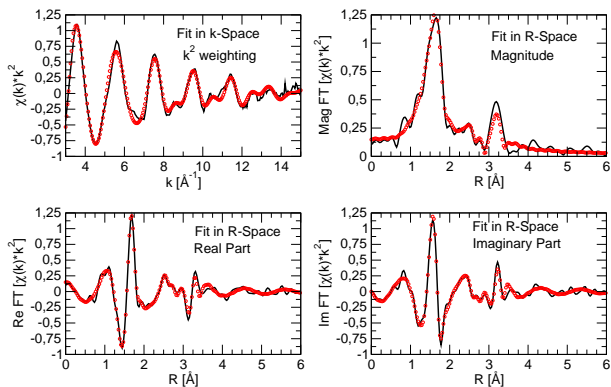
(a) Fit including only single scattering paths. The fit shows deviations from the experimental spectrum above R=3.2 Å (Fourier transformed spectrum).
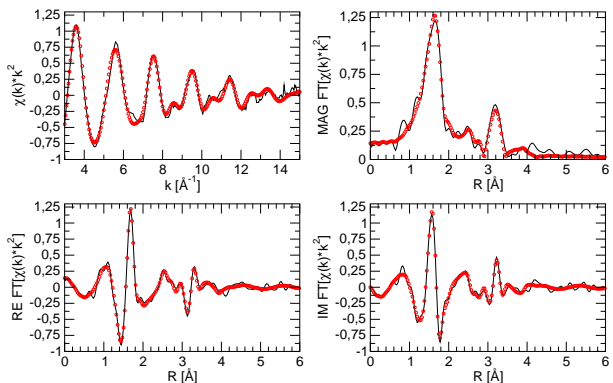
(b) Fit including all relevant multiple scattering paths up to a path length of 4 Å. The fit quality above R=3.2 Å is improved. In the EXAFS function, no significant change is visible. The graphs are arranged in the same manner as in the figure above.

Table 3.4: Results of the full EXAFS analysis of electrochemically grown Au_2O_3

Statistical Parameter	Value
Independent Points	19.5
Number of Variables	13
Degrees of Freedom	6.5
R-factor of Fit	0.004
χ^2	11898
reduced χ^2	609
k Interval	[2.8:16]
R Interval	[1:3.4]

(a) Statistical Parameters.

	General Parameters				
S_0^2	0.74			E_0	15.51
	Path Parameters				
Atoms	Type	R_{nom}	ΔR	σ^2	N
	single or multiple scattering	ideal distance from absorber	distance deviation	Debye Waller Factor	Degeneracy
Au,O	SS	1.929	0.058	0.003	1
Au,O	SS	2.012	-0.026	0.003	1
Au,O	SS	2.042	-0.056	0.003	1
Au,O	SS	2.071	-0.086	0.003	1
Au,O	SS	3.049	-0.019	0.0098	1
Au,Au	SS	3.033	0.011	0.011	1

(b) Variables used in the fit.

EXAFS shows high disorder, no multiple scattering paths contribute to the EXAFS. From table 3.3, the paths 1-4,7 and 8 have been taken into account. Paths Nr. 5 and 6 could not be detected in the EXAFS - a phenomenon which needs further discussion. The two main reasons for this are: (i) the three non-detectable scatterers are low-Z scatterers which are harder to analyse with EXAFS and (ii) the thermal motion of these atoms is so high that the corresponding EXAFS oscillations are damped. Both seem to apply here. Examining the Fourier-transformed EXAFS reveals a very broad signal with a maximum at 1.9 Å but with a strong shoulder towards higher R values. Such structureless features are hard to fit with a Levenberg-Marquardt algorithm. The atoms labelled O5, O6 and O8 (the light blue atoms in fig. 3.12(b)) are not linked to the central gold atom or the one detected in the second shell. All atoms which have been successfully fitted with FEFFIT are linked to each other, i.e. they show a stiff, covalent structure. This is not true for the three non-detectable oxygen atoms. Examining the crystal structure of Au_2O_3 one finds that these three atoms are linked to other gold atoms in the covalent network. During electrochemical oxidation, where dissolution of the gold metal as well as oxygen evolution are the dominating processes (only 1 %

Figure 3.12: EXAFS fit of electrochemically grown Au_2O_3: The fit shows large contributions in the first shell regions. The EXAFS function itself is structureless compared to the one from crystalline Au_2O_3.
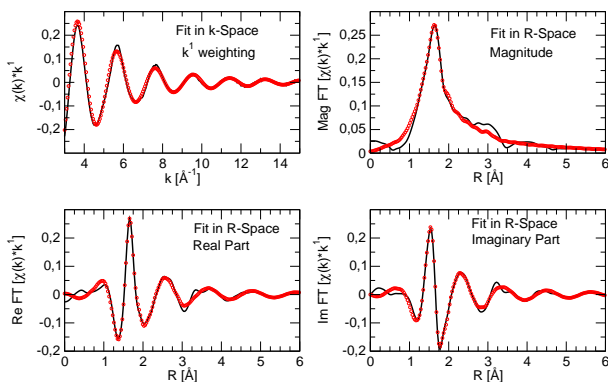

(a) Fitted EXAFS function.
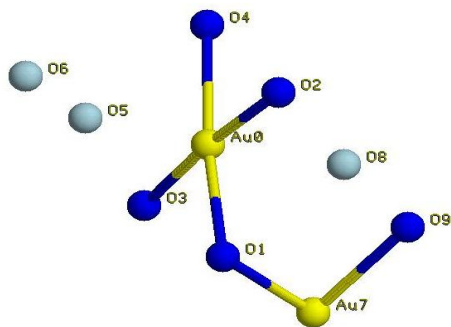
(b) Corresponding structural model. Note that the light blue oxygen atoms (O5, O6, O8) cannot be detected. They are included here for discussion purposes (see text). The EXAFS analysis clearly shows the distorted square planar grouping of oxygen atoms around the central gold atom. As the disorder is high in this system only one additional gold and oxygen atom - belonging to the second square planar structure linked to the central unit *via* a common vertice - are visible.

of the charge passing through the electrode goes into the oxide formation), only small crystallites can be formed, as the strong convection on the surface leads to the breaking of any long range order. It is straightforward to assume that the formation of the oxide terminates at points where the crystal structure can be broken. The cluster formed *via* electrochemical methods seems to be the smallest possible cluster where all atoms are linked to each other *via* covalent bonds.

3.2.5 XAS ANALYSIS OF THE GROWTH PROCESS

Different oxide films were prepared as described previously, the current density has been varied over several orders of magnitude. All samples were galvanostatically oxidised. Figures 3.13 and 3.14 show a typical linear combi-

Figure 3.13: Linear combination analysis of the growth of Au_2O_3 under electrochemical conditions. The current density applied here was 0.5 mA/scm. The good reproducibility of the spectra indicates no intermediate species formed during the oxidation.
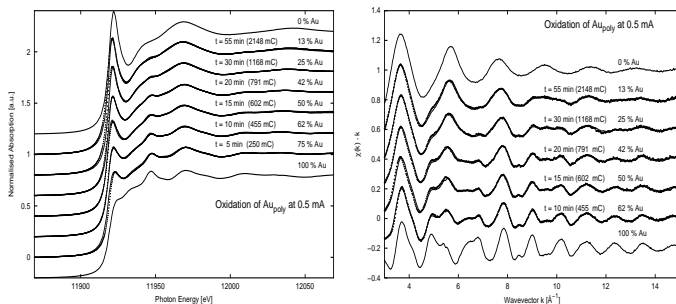
(a) XANES spectra.   (b) EXAFS spectra.

nation analysis of XANES and EXAFS spectra. These LC algorithms were calculated with the XMGRACE program of the Weizmann Institute [87]. It has been tuned in a manner to fit a given spectrum using up to 9 reference spectra. In the case of the oxide growth process, the experimental data was well reproduced with two references, i.e., a gold metal and a gold oxide reference spectrum. This kind of analysis has been carried out with all spectra

Figure 3.14: Linear combination analysis of the growth of Au_2O_3 under electrochemical conditions. The current density applied here was 450 mA/scm.
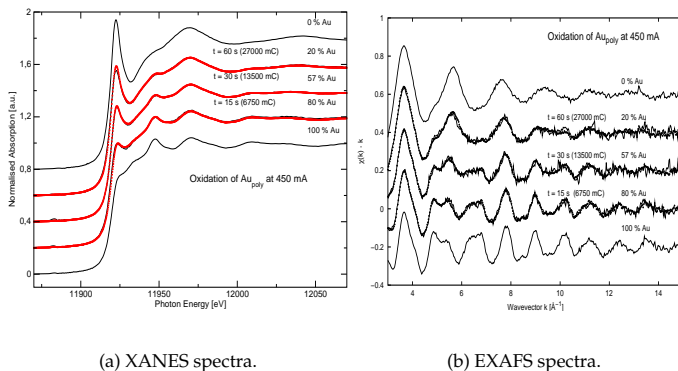
(a) XANES spectra.

(b) EXAFS spectra.

taken during the synchrotron work. The graphs shown here are representative for the fitting quality. As can be seen, the experimental data do not deviate significantly from the linear combined reference spectra. This result was obtained throughout the whole current range from 650 mA to 0.5 mA. For purposes of the XANES analysis, a careful normalisation process was needed. The fact that systematical errors sometimes change the background function of a given spectrum leads to problems in the analysis procedure. Therefore, a *functional* normalisation approach was used to normalise the spectra. Usually, the spectra are normalised by subtracting the pre-edge and setting the edge-step to one. In this analysis, the 2nd order polynomial obtained by calculating the edge step value was used to do a functional normalisation. Systematic errors lead to a non-linear increase in the absorption behaviour of a sample behind the edge. If the post-edge region is divided by the 2nd order polynomial used for determining the edge step, a straight line can be obtained. The algorithms used for this procedure have been provided by the IFEFFIT package written by M. Neville. A comparison between normal and extended fitting procedure showed a significant improvement of the fitting quality. Compared to the linear combination of EXAFS method, the same results could be obtained. Therefore, the application of this algorithm is justified. It should however be mentioned that this normalisation

method is not suitable for a good EXAFS analysis as subtracting of a non-linear background function *can* produce non systematic errors which falsify the analysis. The method described here has therefore only been applied to XANES spectroscopy. As the linear combination method works well in this case, it was worthwhile testing if the same results could be obtained *via* a fitting analysis using the theoretical fitting standards available from FEFFIT. This method will prove to be extremely useful if a system with no known reference compounds is under investigation. A series with a current density of 7 mA/scm was chosen to be analysed *via* FEFFIT. The fitting results are shown in fig. 3.15. This fit is an example of FEFFITs capability of fitting multiple data sets in one run thereby enhancing the available parameter space. The basic principle will be shown here by examining the input file used for this fit. The input file consists of a *global* section and a *local* section. In the global section, the fit parameters (format of files, verbosity, variable declaration) are defined. In the following local sections (separated by the keyword **next data set**), for each individual data set the path definitions are given along with the fitting ranges in k and R-space. The phase composition analysis was achieved by using two paths, namely (i) the first four oxygen atoms of gold oxide and (ii) the twelve nearest neighbours of gold in gold metal. These paths can be combined using the appropriate percentages, which have previously been obtained *via* the LC XANES method. It should be mentioned that fitting the percentages themselves also yielded good results compared with the XANES analysis. The maximum deviation between the two methods is about 4%. In table 3.5, the results from XANES and FEFFIT analysis are summarised. Fig. 3.17 shows the relation between the percentage of Au^0 detected *via* XANES measurements after a background correction of the XANES region with IFEFFIT. From this graph it is visible that all oxidation series show the same oxidation behaviour when relating Au^0 fraction to the charge (related to unit area). This result is in line with literature, where it has been stated that the oxidation of gold proceeds linear with time. If one assumes a growth process obeying the equation $d = c \cdot I \cdot t = c \cdot Q$ and taking into account that the Au(0) intensity is attenuated according to $I = c \cdot exp(-d/\lambda)$ [69,71], this leads one to the fact, that the Au(0) fraction observed in the XANES region must obey the following law:

$$P_{Au} = exp\left(-\frac{c \cdot Q_{ox}}{\lambda}\right) \qquad\qquad (3\text{-}1)$$

Table 3.5: Results of the Phase composition analysis of Au_2O_3 with FEFFIT. The conditions were: I_{ox}=7 mA. For all data sets, the same σ^2, ΔR, E_0 and S_0^2 was applied (Au: σ^2=7·$10^{-3}$$Å^{-2}$, ΔR=-0.01 Å, E_0=6.21, S_0^2=0.87 O: σ^2=3·$10^{-3}$$Å^{-2}$,$\Delta R$=-0.03 Å, E_0=15.85, S_0^2=0.74). The index "F" denotes the FEFFIT procedure, "X" the LC XANES method.

t_{ox} [min]	Q_{ox} [mC]	$P(ox)_F$	$P(ox)_X$	$\Delta P(ox)$	$\Delta P/P$ [%]
13	4961	0.43	0.38	0.05	13
18	6763	0.50	0.50	0.00	0
23	9071	0.57	0.58	-0.01	2
33	13686	0.75	0.75	0.00	0
58	25644	0.82	0.87	-0.05	6

Figure 3.15: Phase composition analysis using FEFFIT. The current density applied in this experiment is 7 mA/scm. The results are in good agreement with the ones obtained *via* the LC methods.
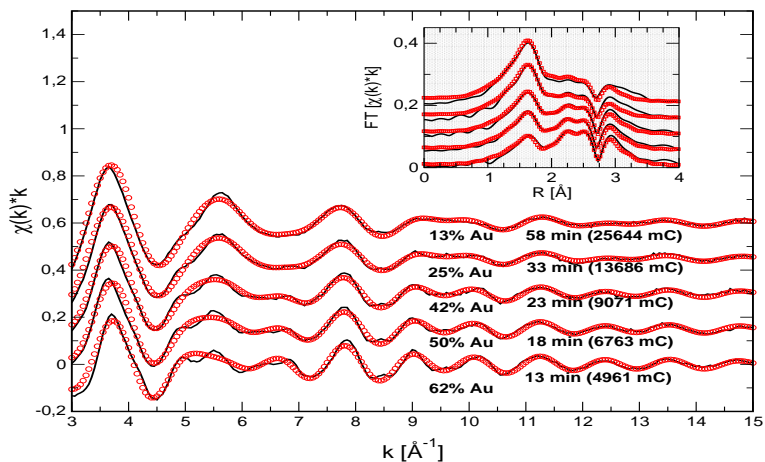
From this equation, the growth constant c can be evaluated. If we use the decay constant for Au_2O_3 ($\lambda = 315$ Å [73]) we obtain a value of c=$1.56 \cdot 10^{-2}$ [Å·scm/mC]. For the Au^{3+} ion, the following data could be obtained from ref. [93]: r(Au^{3+}, KZ=4): 0.82 Å, r(Au^{3+}, KZ=6): 0.99 Å. From fig. 3.6, the linear growth of gold oxide during the oxidation process has already been deduced. The growth constant obtained was $1.2 \cdot 10^{-2}$ [Particles·scm/mC]. If these values are compared to each other, a good agreement can be stated. A direct relation would be difficult, as one cannot say how dense the surface oxide which is formed during the oxidation process really is. But generally, the two values should be in the same order of magnitude, which is perfectly the case here. All results described up to now stem from the analysis of the Au L_3 edge. The same analysis can be carried out for the L_2 and L_1 edges. From the analysis of the three edges, a depth profile could in principle be established as the escape depths of the released electrons vary with kinetic energy of the incident photon beam. Unfortunately, the exponential decay constants seem to be quite similar to each other as can be seen from fig. 3.16, where the results for the 650 mA data sets are shown at the L_2 and the L_1 edge.

### 3.2.6 EXPERIMENTS WITH AN *in situ* FLUORESCENCE CELL

A main interest during the design of the synchrotron cells was to achieve maximum surface sensitivity. GI (grazing incidence) methods are not applicable here as the sample surface is too rough in the case of polycrystalline gold foils. For such studies, single crystals have to be used, but these can be easily damaged by the electrochemical oxidation process. Another method of enhancing the surface sensitivity is to use thin gold films grown on mica as samples. These films can be prepared with defined thicknesses ranging from 50 Å to 1000 Å. The use of such films has been tested but failed due to insufficient adhesive strength. When currents $> 10\,\mu A$ were applied, the gold film peeled off during the oxidation. When films thinner than 250 Å were used, no electrochemical experiments were possible. A thickness of ≥ 1000 Å is too insensitive to allow detection of surface changes. The film thickness of 500 Å used in the test experiments yielded a good electrochemistry, but the formed oxide periodically peeled off the substrate, as can be seen in fig. 3.18. The noise is due to a fast scanning time of ≈ 5 minutes per spectrum. This was the period in which the flaking of the oxide film and later reoxidation of the deeper gold layers was detectable. Also, a high background fluorescence

Figure 3.16: Growth process (I_{ox}: 650 mA) monitored at the L_2 and L_1 edges of Au metal. Only small differences concerning the decay constant are remarkable. The L_2 edge shows a considerably less intense whiteline, the L_1 edge is nearly featureless and therefore difficult to analyse.
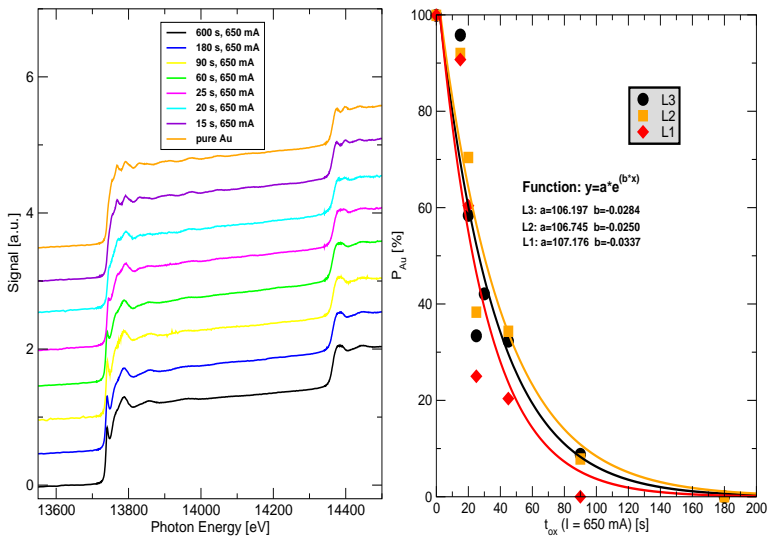
(a) L_2 and L_1 edges

(b) Exponential decay functions

Figure 3.17: Analysis of different galvanostatic oxidation processes. After correction of the flown charges with respect to the area of the electrodes, an exponential falloff in the Au^0 signal can be observed for all series. It is important to note that the P_{Au}/U_t graph shows different falloff constants while the P_{Au}/U_t graph shows one constant for all experimental data.
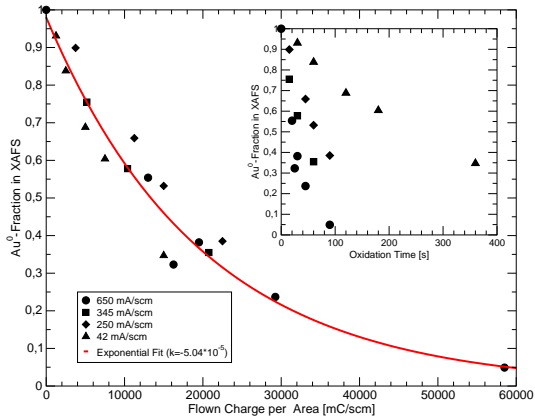
signal due to the mica support and the electrolyte is responsible for the bad S/N ratio.

3.2.7 ANALYSIS OF THE DECOMPOSITION PROCESS

3.2.7.1 Crystalline Au_2O_3

For crystalline Au_2O_3 the decomposition has been monitored by transmission XAS spectroscopy. Additional TPD studies have been carried out to measure the activation energy of this process [42]. The results will not be presented here.

3.2.7.2 Commercial Au_2O_3

The commercial gold(III) oxide has been characterised with the TEY XAS setup. Prior to XAS analysis, thermogravimetric studies have been carried out. A typical TGA spectrum of the commercial gold oxide sample is shown in fig 3.21. A decomposition series with the corresponding TPD results is shown in fig. 3.19. The figure shows a good correlation between the O_2 TPD

Figure 3.18: Test experiments with a cell using a gold/mica film as electrode. The cell used consists of a Teflon body equipped with counter and reference electrode as well as a Viton sealed gold on mica film as working electrode. The X-rays pass through the mica and excite the gold atoms of the film. A 45° geometry assures that the fluorescence reaches the detector. Measurements have been carried out at beamline X1, HASYLAB at DESY.
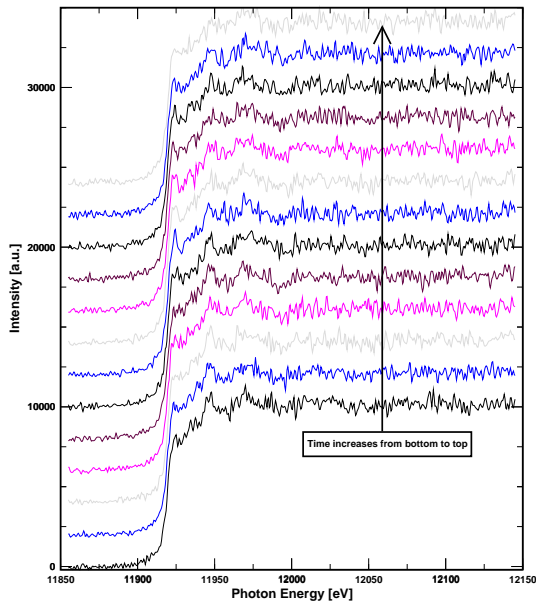

signal and the Au^{3+}/Au^0 ratio calculated from EXAFS spectroscopy. In fig. 3.20 (a) the linear combinations are shown. The figures compare the decomposition of commercial and electrochemically grown oxide. Results for the commercial oxide are also in line with the TGA analysis. When comparing the two samples, a similar decomposition behaviour can be detected. Note that for the commercial available oxide, the temperature has been held constant over a certain period of time.
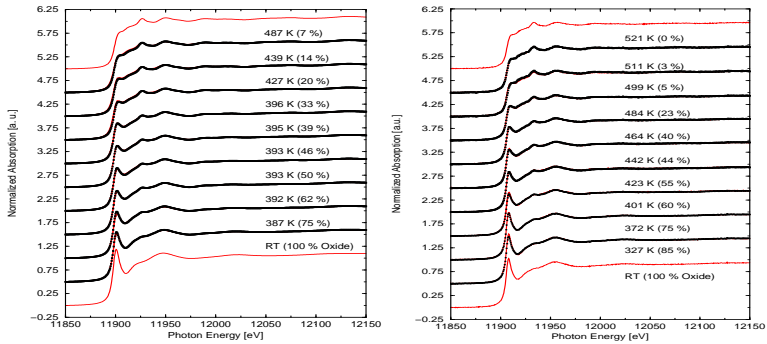
3.2.7.3 Electrochemically Prepared Au_2O_3

The electrochemically prepared samples were transferred into the TEY XAS cell shown in fig. 2.10. Great care has been taken to transfer the samples

Figure 3.19: Decomposition of commercial Au_2O_3 as measured by XANES spectroscopy and TPD. Both methods yield similar results. The turnover point determined *via* the XANES linear combination technique is in good agreement with the maximum of the TPD.
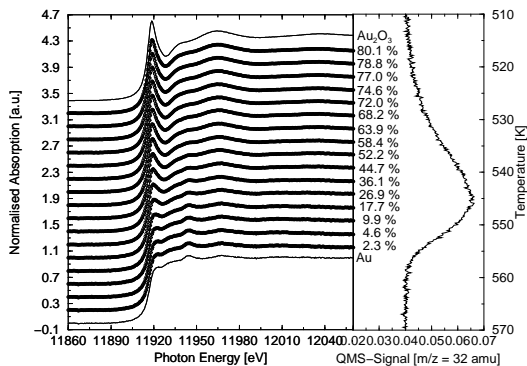

under inert gas, but as the mounting of the cell is complicated, the possibility of O_2 coming in contact with the sample cannot be excluded. The cell was flushed with a He stream (50 ml/min). Figure 3.22 (b) shows the NEXAFS region of the Au L_3 edge during heat up of an oxidised gold foil. The oxidation conditions were chosen in a way that the oxide dominates the depth region of the electron origination depth (about 1000 Å). As one can see, the white line (characteristic feature for Au^{3+} in the oxide compound) gradually decreases until at about 500 K no whiteline is visible. It is quite useful to compare the NEXAFS spectra with the corresponding Fourier transformed EXAFS spectra shown in fig. 3.22 (a). While the NEXAFS region shows a gradual decrease of the white line (which is a measure of vacant d states in the sample), the Fourier transformed EXAFS shows a decreasing contribution at R=2 Å. This correlates with the loss of oxygen scatterers at this distance. These pictures are a good illustration of the fact that NEXAFS measures the changes in the electronic structure while EXAFS monitors the structural changes in the sample. To analyse the percentage of oxide present at a given temperature, the linear combination method was applied. The results are shown in fig. 3.20. As for the commercial oxide, each spectrum can be reproduced *via* a linear combination of the reference compounds. In fig. 3.20(c) the decomposition behaviour of the three mentioned Au_2O_3 samples

Figure 3.20: Thermal decomposition of commercial and electrochemically prepared gold(III) oxide monitored by a linear combination of XANES spectra. Top and bottom spectra are the reference compounds used for this analysis (i.e. pure oxide and pure gold metal). It can be seen that at any stage of the decomposition the XANES region can be fitted by a linear combination of the two reference compounds.

(a) Commercial Au_2O_3.

(b) Electrochemically prepared Au_2O_3.
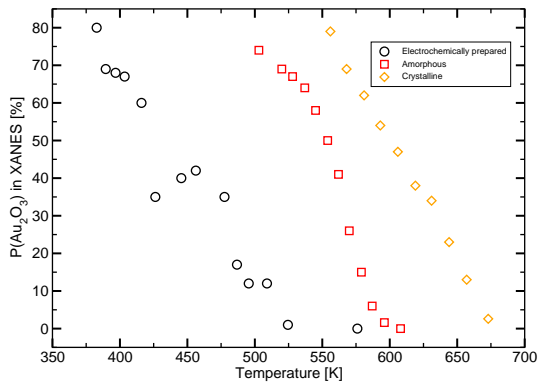
(c) Comparison of the thermal decomposition of three different Au_2O_3 samples. The different decomposition temperatures are clearly visible.

Figure 3.21: TGA analysis of commercial Au_2O_3. Scanning speed was 5 K/min. Mass loss sets in slightly above room temperature. The steady loss between RT and 500 K is attributed to the loss of water. O_2 evolution starts at about 520 K and ends at 560 K. The TGA results are consistent with TPR experiments carried out additionally.
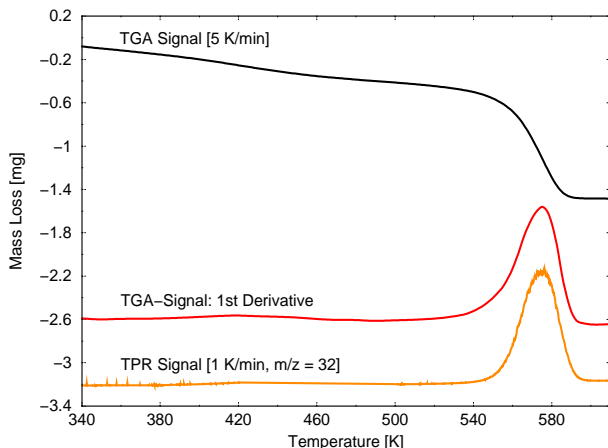

are compared to each other.

3.3 TPD Experiments

As already pointed out in the previous sections, thermal desorption spectroscopy provides an easy access to thermodynamic data on the system under investigation. TPD is therefore a good addition to the XPS experiments which provide electronic information and to the structural information obtained from XAS.

3.3.1 TPD EXPERIMENTS WITH O / AU PHASES OBTAINED BY EXPOSURE OF AU TO OXYGEN PLASMA DISCHARGES

From literature it is well known that oxygen plasmas as well as reactive molecules as O_3 or NO are capable of oxidising gold at least partially [41, 46, 47, 58, 59, 65]. However, a systematic TPD study is still lacking. This section

Figure 3.22: Spectra taken during the thermal decomposition of electrochemically prepared Au_2O_3.
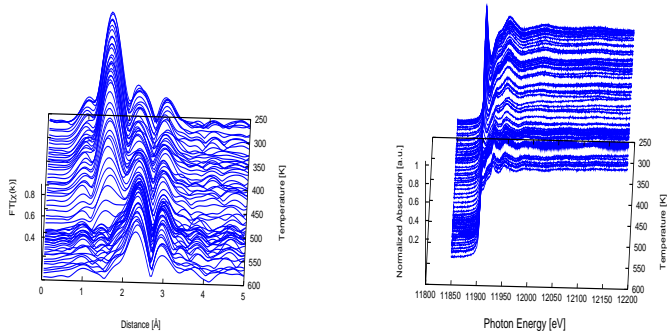
(a) Fourier transformed spectra. The spectra at low temperatures show a large FT contribution at R=2 Å which gradually decreases as the temperature rises. Decomposition sets in already shortly above RT. At T=500 K, Oxide contribution can no longer be observed.

(b) NEXAFS spectra acquired during the thermal decomposition of Au_2O_3. These spectra show a strong whiteline at room temperature corresponding to the original oxidic state which is gradually decreasing during heat-up.

therefore deals with the investigation of different O_2 plasma conditions on the formed oxides. Fig. 3.23 shows the influence of the sputtering time on the evolution of the O_2 TPD signal. From this graph it is evident that first a state (hereafter labelled γ_2) at T$\approx$ 510 K (at β=3.71 K/s) is populated. Even a sputter time as short as one second is capable of producing this state. A heating rate variation experiment yields a desorption energy of 131 kJ/mol which is perfectly in line with the results obtained from a Redhead analysis. With increasing exposure time, a state at $\approx$360 K appears (hereafter referred to as γ_1). This is not a sharp peak but a slight increase of the TPD baseline. It is therefore very difficult to analyse. A Redhead evaluation with T_{des}=360 K yields a desorption energy of 43 kJ/mol. With further increase in exposure time, a shoulder growth on the high temperature side of the γ_2 peak is observed. A heating rate variation experiment here yields a

desorption energy of 133 kJ/mol. A Redhead analysis yields 143 kJ/mol, a discrepancy which can be tolerated. This peak (further referred to as β_2) can be attributed to oxidic oxygen in the sample. This is proven by the fact that TPD experiments with electrochemically prepared samples yield one peak at exactly this temperature with the same desorption energy. A further comparison with Gottfried's [19] results shows a strong similarity between the position and desorption energy of this peak with the β_2 state he finds by irradiating physisorbed oxygen with UV light or electrons. The last state formed - which only appears at high exposure times - is labelled γ_3 for future reference. It is quite broad and therefore, an exact peak position is difficult to find (esp. for low heating rates). This might be the case why for this peak, Redhead and heating rate variation methods differ quite a lot from each other (Redhead: E_{des}=173 kJ/mol with T_M=660 K; HRV: E_{des}=116 kJ/mol). In this case, the Redhead evaluation seems to yield the better result. The results for the heating rate variation are presented in fig. 3.24. The influence

Figure 3.23: The influence of sputtering time on the m/z=32 signal measured in TPD. The first state populated is the γ_2 state, followed by γ_1, β_2 and γ_3.
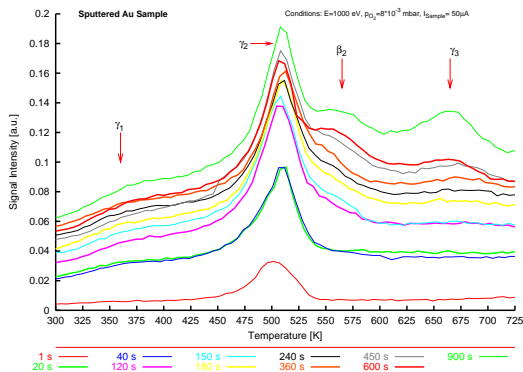
of the sputter energy was also investigated. In fig. 3.25, the heating rate variation experiment for two different energies is shown. Interestingly, the sputter energy seems to have no influence on the formed oxygen species as both experiments yield the same value for E_{des}. Also, a sputter energy of zero (i.e. a pure exposure of the sample to an oxygen plasma) yielded the TPD states mentioned above. Therefore, a value of 1 keV was chosen for all future experiments.

Figure 3.24: Heating Rate Variation experiment carried out with a sample exposed for 900 s to an oxygen plasma discharge (p_{O2}=3·10^{-8} mbar, E=1 keV).
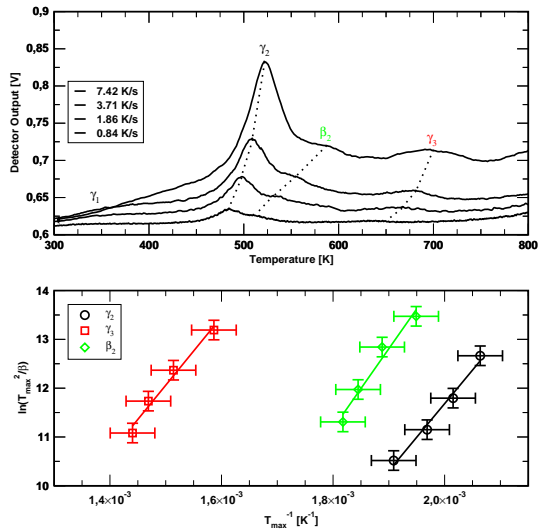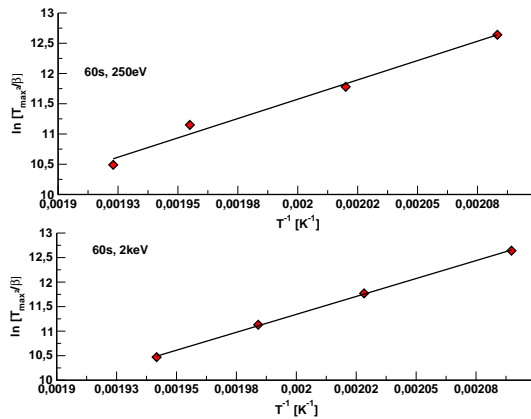

Figure 3.25: Heating rate variation for different sputter energies. Note that the desorption energy is nearly equal in both cases.

### 3.3.2 Experiments with Electrochemically Prepared O/Au Phases

In fig. 3.26 TPD spectra of a galvanostatically and a potentiostatically oxidised sample are shown. One can see that a change in the oxidation method does not affect the position and shape of the O_2 signal formed by thermal desorption. In the potentiostatic case, below 1.75 V no oxygen signal is visible, while in the galvanostatic case a minimum current of 35 μA has to be applied to oxidise the sample. Fig. 3.27 shows heating rate variation exper-

Figure 3.26: TPD experiments with different gold samples after potentiostatic and galvanostatic oxidation.
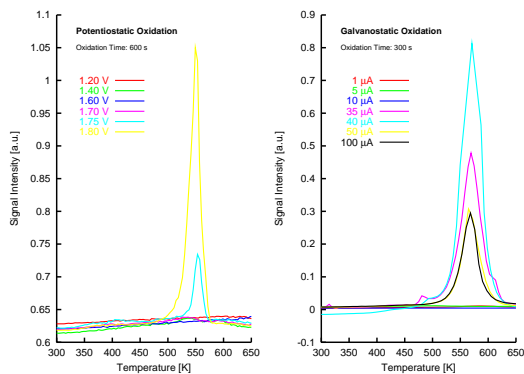
iments with these samples. For the galvanostatic case only two spectra are available. Comparing these to the potentiostatic case, one concludes that the peaks look quite similar. Fig. 3.28 shows the TPD spectra for different m/z values. From this figure, the most important source of problems during these UHV studies is evident: impurities (C and H_2O) on the sample produce peaks with other m/z values. The m/z=16 TPD shows a steep increase of the signal slightly above RT which is certainly due to desorption of water molecules from the sample and its surroundings. The corresponding OH and H_2O TPD spectra are not shown here, but their shape is essentially the same. The partial pressure of water is therefore very high in the analysis chamber during these experiments. Liquid nitrogen traps and titanium sublimation pumps improve the pressure during the experiments but were found to be insufficient to remove all water molecules. The carbon impurities (found on

Figure 3.27: Heating rate variation experiments with galvanostatically and potentiostatically oxidised samples.
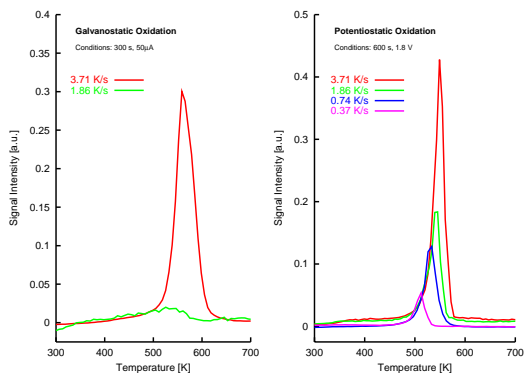
all samples after transferring from electrochemical to UHV part) produce CO and CO_2 peaks - obviously generated by reaction of these impurities (which stem from the residual pumping oil in the roughing pump stage) with oxygen of the oxidic compound.
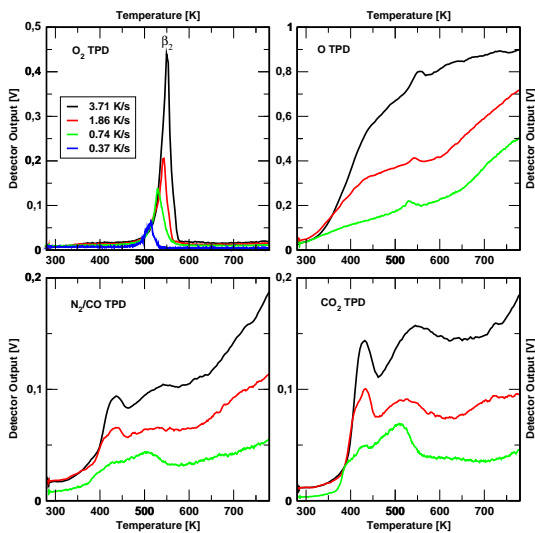
3.4 XPS Experiments

3.4.1 EXPERIMENTAL

All data shown in this chapter have been obtained with the following equipment:

1. A Leybold X-ray source (RQV 60) operating at 300 W power (constant power mode). The emission current has been set to 20 mA, the acceleration voltage to 15 kV. Under these conditions, no decomposition of the surface compounds were detected within the time range of the experiments.

2. A PS-EA10 hemispherical electron analyser (SPECS). The spectrometer always operated at CCR mode, pass energy has usually been set to 20 eV. Under these conditions, the Au $4f_{7/2}$ line shows a FWHM of 1.2 eV. This resolution is good enough to analyse contributions of Au^{3+} to the XP spectra because the 4f lines of the two states are separated by about

Figure 3.28: TPD spectra acquired for different m/z values after a potentio-static oxidation at 1.8V

1.6 eV [11, 41, 47, 60, 65]. The O 1s line has a larger FWHM so that the spectrometer is also capable of analysing the O 1s lines of oxygen.

During all experiments, the sample surface was analysed by XPS before preparation, to ensure that it was in a clean state. Experiments were only carried out if no Ca, C or O impurities were detected on the surface. The problem of Ca evolution from the bulk material was not observed in this thesis. After the electrochemical or plasma treatment the sample was characterised using the Au 4f, O 1s and Au $4p_{3/2}$ Signals. For peak parameter analysis, the program XPSPEAK was used. It uses an implementation of the Levenberg-Marquardt algorithm to fit the experimental data by a linear combination of background signal and a number of Gauss-Lorentz curves. During the fitting process, all parameters were kept constant except the peak area. The Gauss/Lorentz (G/L) ratio was determined independently by fitting the Cu 2p region of a pure copper foil and the Au 4f signals of pure gold foil. This value is solely determined by the X-ray source and the spectrometer and was thus not changed during fitting procedures. The FWHM value for the Au 4f peaks were determined by fitting spectra of pure gold metal. For Au^{n+} con-

Table 3.6: Summary of all peak parameters applied during the forthcoming analysis.
Superscript denotes the oxidation state (only given for gold). Subscript denotes the different preparation methods (sp - sputtering, el - electrochemical)

Element	Region	Peak Number	Binding Energy [eV]	FWHM [eV]	G/L [%]
Au^0	4f	1	84.0	1.13	50
Au^{3+}	4f	2	85.6	1.13	50
Au_2^{3+}	4f	3	86.4	1.13	50
Au^0	4p	1	546.2	4.68	50
Au^{3+}	4p	2	547.8	4.68	50
O_{sp}	1s	1	529.3	1.82	50
O_{sp}	1s	2	530.8	1.82	50
O_{el}	1s	1	530.0	1.82	50
O_{el}	1s	2	531.8	1.82	50
O_{el}	1s	3	533.1	1.82	50

tributions, the FWHM was not changed. The FWHM value for the Au 4p region was determined in the same manner. For the O 1s region, a sample was exposed to a very short plasma discharge where the formation of only one species was expected. The FWHM value for this peak was used throughout the analysis. In table 3.6 the peak parameters of all applied G/L curves are summarised for later reference. Thermal decomposition was also followed with XPS. Depth profiles (ARXPS) were acquired for some selected preparation methods. To carry out meaningful experiments, first the influence of the UHV conditions on some selected electrochemically prepared samples was inspected (fig. 3.29). This investigation shows that electrochemically prepared oxide films are to a small extent sensitive to the UHV conditions. This seems reasonable, as UHV usually has a reducing effect on materials. Therefore, an oxidic compound may be partially reduced when inserted into the UHV recipient. The figure below shows that this influence - although existent - is small on the timescale of a typical XPS experiment. Typical XPS data acquisition times were about 15 minutes per spectrum. From the data shown below one can state that the reducing effect sets in after a few hours. All experiments were therefore carried out as quickly as possible with a reproducible transfer procedure.

Figure 3.29: UHV decomposition of an electrochemically prepared Au$_2$O$_3$ phase. It is clearly visible that the reducing atmosphere of the UHV influences the chemical composition of the sample. However, on the time-scale of a typical experiment, the effects visible here are negligible
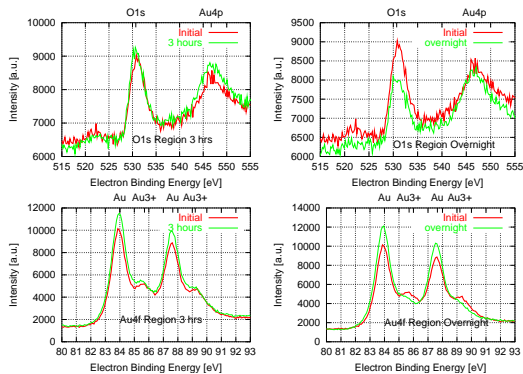

3.4.2 XPS Studies of Au/O-Phases Obtained with a Plasma Discharge

The influence of exposure time, ion energy and O$_2$ partial pressure has been investigated. Figure 3.30 shows the initial stage of oxygen deposition as seen by XPS. The oxidation times are all below 60 s. This experiment was carried out to investigate the growth rate of the oxygen signal. From the graph it can be seen that no changes in the spectra are visible in the time range from 15 to 60 s. Shorter sputter times are hard to achieve because the discharge must be ignited and the pressure must be controlled during the process.

In nearly all cases, the XP signals in the O 1s region could be fitted with one G/L curve (O$_{sp}$ 1). In some experiments (at high sputter times) a second contribution could be detected (O$_{sp}$ 2). No correlation between experimental parameters and the appearance of this peak could be established. It could be that at high exposure times, the surface is saturated with the first species and a second one is formed afterwards. The TPD data presented in this thesis show that under the conditions of the XPS experiments (E=250 eV, p=8·10^{-3} mbar), the XP peaks vanish at temperatures above the γ_2 peak in the TPD data. A possible interpretation of this fact is that the peaks visible *via* XPS can be attributed to this state. Its binding energy corresponds to a high oxidation state. It can be concluded that the γ_2 state consists of oxidic surface oxygen.

Figure 3.30: XP spectra of polycrystalline gold samples exposed for short times to a 250 eV plasma discharge.
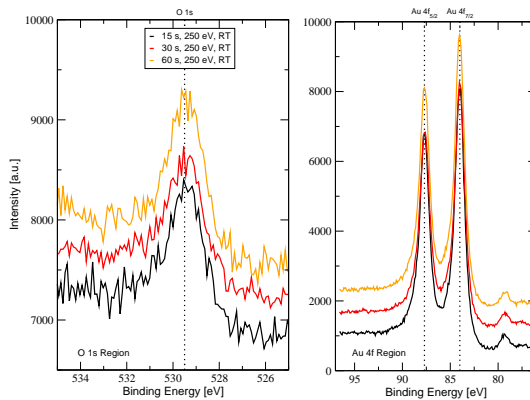
This fact is also supported by CO titration experiments. A selection of XPS experiments with plasma oxidised samples under CO atmosphere are shown in figs 3.31 and 3.32. To show the quality of the fitting procedure, fig. 3.33

Figure 3.31: Influence of CO on the XP spectrum of a plasma oxidised Au sample. The black spectrum was acquired after 15 minutes of O_2 plasma exposure at E=250 eV. The dotted line is the spectrum acquired directly after adding CO at RT.
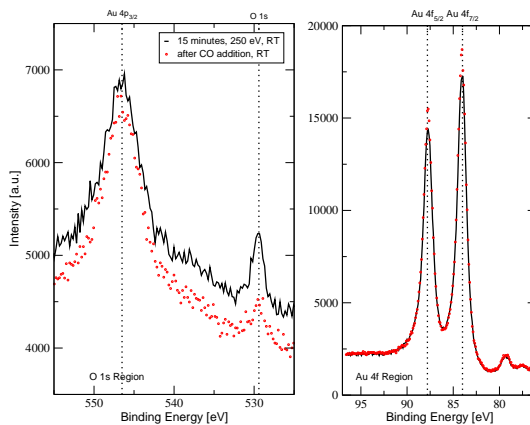
Figure 3.32: Influence of CO on the decomposition of oxidic oxygen species prepared *via* the plasma oxidation method. It is visible that the addition of CO to the residual gas in the recipient immediately reduces the intensity of the O 1s component in the XP spectra. Also, the intensity of the Au 4f signal increases which can be interpreted as the removal of surface oxygen species.
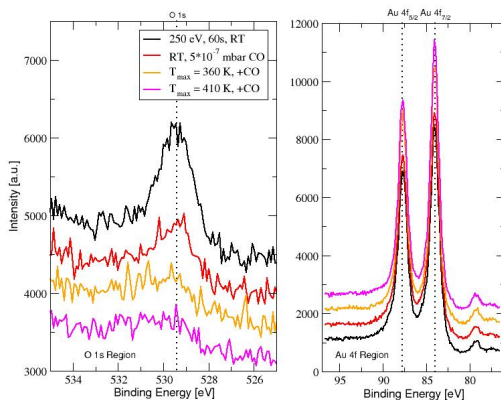

shows fitted spectra of a gold sample exposed to a 250 eV O_2 plasma for 5 minutes. The O 1s region can be fitted with one Gaussian while the Au 4f region shows contributions from a second Au 4f signal in addition to the Au 4f line at 84.0 eV.

3.4.3 XPS STUDIES OF AU/O-PHASES OBTAINED BY ELECTROCHEMICAL OXIDATION

For all oxidation procedures, the surface state of the clean electrode was characterised *via* XPS and CV. The oxidation profiles have been recorded to evaluate the charge passed through the system during the oxidation. The transfer procedure was to (i) move the sample after oxidation into the roughing pump stage for 15 minutes, (ii) move it to the HV stage for 30 minutes and (iii) transfer it to the analysis chamber. A typical XPS experiment with all stages from cyclic voltammetry to XPS characterisation is shown in fig. 3.34. A different decomposition series is shown in fig. 3.35. The electrochemical oxidation of a polycrystalline gold surface leads to three distinguishable oxygen states (see table 3.6). The binding energies of these states (530.0, 531.8 and 533.1 eV) correspond to a highly oxidic

Figure 3.33: XPS peak fits of a gold oxygen phase obtained *via* a plasma discharge. The conditions were: E=250 eV, t_{ox}=5 min. The addition of CO leads to a significant decrease in the O 1s signal intensity. However, only heating removes the surface state completely. The spectra show (from bottom to top) (i) the sample at RT without CO, (ii) the sample at RT after adding CO, (iii) the sample after heating in CO to 350 K and (iv) the sample after heating in CO to 460 K.
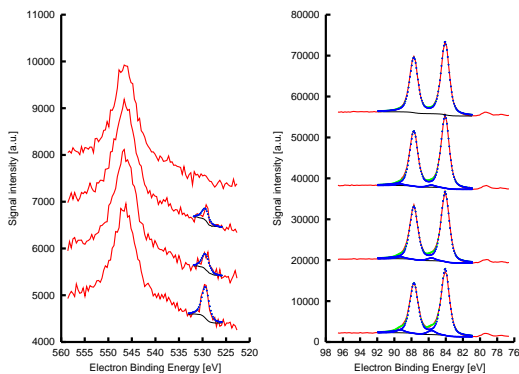
(530.0 eV), a hydroxydic (531.8) and an aqueous/hydrous (533.1 eV) state. These assignments have been made after consolidating tables with typical BE values of certain oxygen containing materials. In all XP data analysis procedures, these three states could be detected. The thermal decomposition of electrochemically grown Au_2O_3 monitored *via* XPS yields the following results:

- At room temperature, all three peaks are visible in the spectrum. The relative intensities depend on the oxidation conditions, but no trend can be observed. It is generally the case that the hydroxydic (531.8 eV) state is the most dominant one at room temperature. The oxidic and hydrous states (530.0 and 533.1 eV) are less intense.

- Upon heating, the oxygen contributions gradually decrease in intensity. This leads to a lowering of the O_{tot}/Au ratio.

- Also during the heat up process, the ratios of the different peaks to each other change drastically. It has been observed during all experiments that the oxidic state vanishes at low temperatures (usually below 350

Figure 3.34: A typical XPS experiment following the potentiostatic oxidation of an Au sample. The top left figure shows the state of the electrode before oxidising (CV), the top right one the oxidation I/t profile.
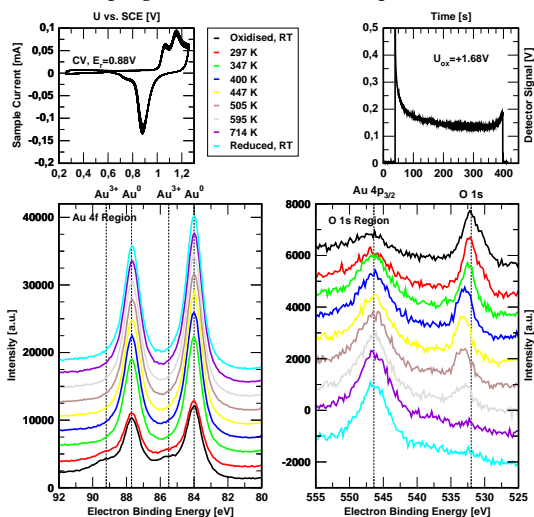

Figure 3.35: Thermal decomposition of an electrochemically prepared oxide layer. The preparation conditions were: Potentiostatic oxidation, U_{ox}=+1.7 V, t_{ox}=600 s. During the heat up process (which has to be carried out stepwise due to the XPS experiments) a constant decrease in the intensity of the Au^{3+} signal as well as a peak shift from low to high BE values of the O 1s peak is visible.
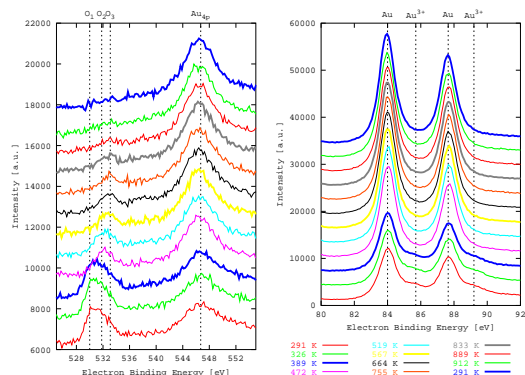
K), while the hydroxydic species vanishes at ≈ 400 K. The most thermally stable state is the hydrous one which is still detected at temperatures as high as 700 K.

- Adding a partial pressure of CO to the residual gas in the analysis chamber immediately leads to a decrease in the O 1s intensity. The thermal decomposition of the oxidised surface proceeds faster.

Figure 3.36: Decomposition of a galvanostatically prepared Au$_2$O$_3$ phase. In these two figures, the decomposition behaviour is shown with and without CO present in the chamber. The oxidation conditions in both cases were: galvanostatic mode, I$_{ox}$=40 μA, t$_{ox}$=300 s.
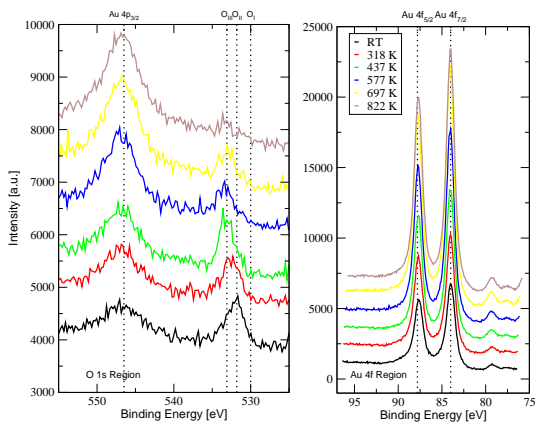
(a) without influence of CO.
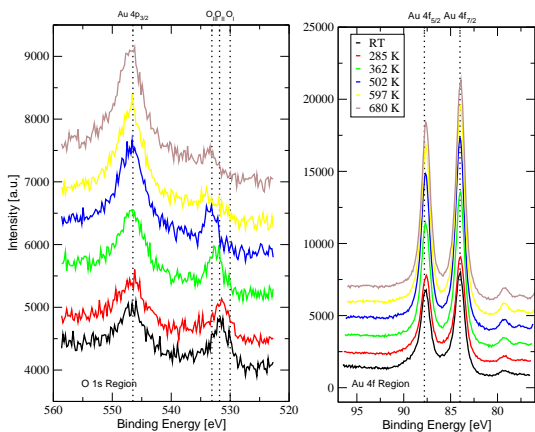
(b) after addition of $5\cdot10^{-7}$ mbar CO.

These results are quite interesting concerning the stability of oxygen phases formed on gold surfaces. When comparing the thermal stability of the oxidic peak to the ones found during O_2 plasma exposure, a similar behaviour can be detected. Both states seem to exhibit the same thermal stability and show similar binding energies. Hydroxidic compounds have not been detected in the case of plasma oxidations - a result which is in line with the literature up to now. However, these species - especially the hydrous one - show a very high temperature stability. This result at first seems to be dubious but can be explained by taking a closer look at the processes which occur during the oxidation processes. As already mentioned, the oxidation process itself is only a side effect in the potential range evaluated in this thesis. The dominant processes are oxygen evolution and gold dissolution. Therefore, the electrode material is under constant roughing conditions which facilitates the penetration of bulk material by oxygen species. Au-OH and Au-H_2O species may not be stable in the surface regime, but this is surely different if one looks at the bulk properties. For the pure oxidic species, it is known that this material is very sensitive to decomposition to O_2 and Au. The O_2 formed during this process might leave the bulk faster than OH or H_2O species. This would account for the fast decomposition of the oxidic species and the high temperature resistance of the hydroxidic or aqueous species. OH species are likely to form water which is certainly not as mobile in the bulk as oxygen is. EXAFS investigations of electrochemically formed oxide show that the oxidic contributions to the EXAFS vanish at about 520 K. These species are bulk oxides prepared by total oxidation conditions. This may account for the fact that the oxidic and hydroxidic species vanish faster in the XPS experiments. The EXAFS results also show that electrochemically prepared oxides decompose faster than the crystalline analogon. It is reasonable to assume that the incorporation of hydroxidic or hydrous compounds into the bulk destabilises the oxide and favours its decomposition. To demonstrate the quality of the XPS data fits, one thermal decomposition series is shown in fig. 3.37 with the corresponding fits.

3.4.4 EVALUATION OF THE FILM THICKNESS *via* ARXPS

It has been attempted to carry out angle resolved XPS experiments. However, two factors lead to non-negligible errors in these experiments:

1. The fact that the sample is mounted slightly above the optical axis of the transfer rod. While turning the rod and adjusting the angle, a

Figure 3.37: XPS peak fits of an electrochemically oxidised gold foil. The oxidation conditions were: U_{ox}=1.7 V, t_{ox}=300 s. Three oxygen states can be detected at RT. The oxidic one (lowest BE) vanishes first, the hydroxidic and hydrous one follow subsequently.
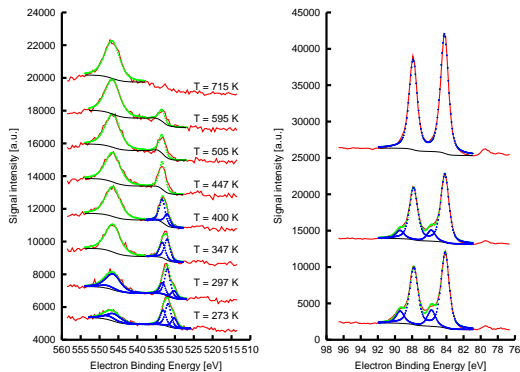
different area of the sample will be irradiated. Furthermore, the sample is turned away from the spectrometer. Although it can be assumed that the electrochemically prepared films are homogeneous, this fact imposes a large error on these data sets.

2. The sample applied is a polycrystalline gold foil which has to be mounted on a stainless steel sample holder. The sample mounting inevitably leads to inhomogeneities of the sample surface. Especially the thermocouple wire, which is mounted directly beneath the gold foil, forms a light elevation on the sample surface. This means that the surface is not flat - an important factor which also imposes errors on ARXPS data.

Table 3.7: Oxide film thicknesses evaluated from ARXPS.

Sputter time [min]	Sputter Energy [eV]	Film Thickness [Å]
60	1000	8.0
45	1000	7.8
20	1000	6.8
10	1000	5.0
5	1000	5.0
2	1000	5.0
Oxidation time [min]	Oxidation Voltage [V]	Film Thickness [Å]
10	1.2	11
10	1.4	18
10	1.6	21

According to the equation described in the theoretical discussion of the methods, basically the thickness and a scaling factor accounting for orbital symmetries, absorption cross sections etc, influence the quality of the fit. For different plasma oxidised samples and for one electrochemical sample, the thickness d has been determined. These results should be treated with care, always keeping in mind the errors mentioned earlier. However, the data shows a consistent trend. It would however be too doubtful to elucidate a growth mechanism *via* these experiments. A better modification of the sample holder or the use of gold single crystals should solve this problem. The results of the analysis of the ARXPS data are shown in table 3.7. The most striking information is that between 2 and 10 minutes, the film thickness does not change. However, according to the large errors mentioned before, this could be due to systematical errors. For the potentiostatically oxidised Au samples, a rapid growth is visible when changing the oxidation voltage from 1.2 to 1.4 V.